Journal of Solid State Chemistry 181 (2008) 1571–1581

Contents lists available at ScienceDirect

Journal of Solid State Chemistry

journal homepage: www.elsevier.com/locate/jssc

Nonaqueous synthesis of metal oxide nanoparticles: Short review and doped titanium dioxide as case study for the preparation of transition metal-doped oxide nanoparticles

Igor Djerdj [a,*], Denis Arčon [b,c], Zvonko Jagličić [d,e], Markus Niederberger [a,*]

[a] ETH Zürich, Department of Materials, Wolfgang-Pauli-Strasse 10, 8093 Zürich, Switzerland
[b] Institute Jožef Stefan, Jamova 39, 1000 Ljubljana, Slovenia
[c] Faculty of Mathematics and Physics, University of Ljubljana, Jadranska 19, 1000 Ljubljana, Slovenia
[d] Institute of Mathematics, Physics and Mechanics, Jadranska 19, 1000 Ljubljana, Slovenia
[e] Faculty of Civil and Geodetic Engineering, University of Ljubljana, Jamova 2, 1000 Ljubljana, Slovenia

ARTICLE INFO

Article history:
Received 8 February 2008
Received in revised form
31 March 2008
Accepted 11 April 2008
Available online 30 April 2008

Keywords:
Nonaqueous synthesis
Metal oxides
Nanoparticles
Doped titania

ABSTRACT

The liquid-phase synthesis of metal oxide nanoparticles in organic solvents under exclusion of water is nowadays a well-established alternative to aqueous sol–gel chemistry. In this article, we highlight some of the advantages of these routes based on selected examples. The first part reviews some recent developments in the synthesis of ternary metal oxide nanoparticles by surfactant-free nonaqueous sol–gel routes, followed by the discussion of the morphology-controlled synthesis of lanthanum hydroxide nanoparticles, and the presentation of structural peculiarities of manganese oxide nanoparticles with an ordered Mn vacancy superstructure. These examples show that nonaqueous systems, on the one hand, allow the preparation of compositionally complex oxides, and, on the other hand, make use of the organic components (initially present or formed *in situ*) in the reaction mixture to tailor the morphology. Furthermore, obviously even the crystal structure can differ from the corresponding bulk material like in the case of MnO nanoparticles. In the second part of the paper we present original results regarding the synthesis of dilute magnetic semiconductor TiO_2 nanoparticles doped with cobalt and iron. The structural characterization as well as the magnetic properties with special attention to the doping efficiency is discussed.

1. Introduction

Most of the research in the broad field of *Nanoscience* is dedicated to the development of synthesis routes to nanoparticles and nanostructures. These efforts gave access to nanomaterials with a wide range of compositions, monodisperse crystallite sizes, unprecedented crystallite shapes, and with complex assembly properties. But in spite of all the progress, the most synthesis methodologies were found on an empirical basis, i.e., by trial-and-error experiments, representing isolated efforts without any generally valid basic concepts or mechanistic principles that would allow a rational synthesis strategy. The synthetic chemist is still far away from preparing a certain compound on the nanoscale with a desired composition, structure, size and shape, or even properties, intentionally and in a predicted way. The reasons for this major limitation are manifold and in here we will discuss some of these issues in the context of liquid-phase routes to metal oxide nanoparticles, because their synthesis and application is of particular scientific and technological interest.

In contrast to the traditional high temperature preparation of bulk metal oxides, involving the reaction of a mixture of powders, the use of liquid-phase routes bears the advantage that it is possible to obtain metastable materials, to achieve superior compositional homogeneity, and to influence the particle morphology during the chemical transformation of the molecular precursor to the final oxidic network [1]. Especially aqueous sol–gel chemistry was highly successful in the synthesis of bulk metal oxides [2]. However, it turned out that a specific synthesis route, which worked well for the bulk oxide, cannot directly be adapted to its corresponding counterpart on the nanoscale. The reason lies in the fact that aqueous sol–gel chemistry typically leads to amorphous precipitates that are transformed into the desired crystalline material by applying a calcination step. Due to uncontrolled crystal growth, this temperature treatment to induce crystallization is not a viable option for size- and shape-controlled nanoparticle synthesis. Furthermore, aqueous sol–gel chemistry is rather complex, mainly due to the high reactivity of the metal

* Corresponding authors. Fax: +41 44 632 11 01.
E-mail addresses: igor.djerdj@mat.ethz.ch (I. Djerdj), markus.niederberger@mat.ethz.ch (M. Niederberger).

0022-4596/$ - see front matter © 2008 Elsevier Inc. All rights reserved.
doi:10.1016/j.jssc.2008.04.016

oxide precursors and the double role of water as ligand and solvent, complicating the synthesis of small structures. Nevertheless, several recent examples reported in the literature indicate that it is in general possible to prepare metal oxide nanoparticles in aqueous medium in a controlled way given that the experimental conditions are strictly kept [3–6].

A simple way to circumvent many problems of aqueous chemistry is to perform the synthesis procedure in organic solvents under exclusion of water. The rapidly growing number of publications in this field suggests that these so-called nonaqueous (or nonhydrolytic) processes are particularly successful for the size- and shape-controlled preparation of colloidal inorganic nanoparticles [7–9]. In surfactant-controlled approaches the precursor molecules are transformed into the nanocrystallites in the presence of stabilizing surfactants in a typical temperature range of 250–350 °C [7,8,10], whereas solvent-directed processes just involve the reaction of metal oxide precursor(s) with a common organic solvent and usually take place at lower temperature (50–250 °C) [11–13]. The small number of reactants (precursor and solvent) makes it possible to study the chemical mechanisms involved in metal oxide formation through the characterization of the organic by-products [11]. Parallel to the formation of the inorganic nanoparticles, also the initial organic species (i.e., solvent and/or the organic part of the precursor) undergo transformation reactions. In many cases, the formation of the organic compounds can easily be correlated to the growth of the inorganic nanoparticles, which means that chemical reaction pathways for inorganic nanoparticles can be elaborated based on the organic side reactions [11,14]. The main function of the organic species is to act as oxygen source for the oxide formation, however they are actively involved during all stages of particle growth and crystallization, strongly influencing the composition, size, shape, and surface properties of the nanocrystals [14].

Another important advantage of nonaqueous sol–gel processes in comparison to aqueous systems is the accessibility of ternary, multi, and doped metal oxide nanoparticles [13]. The different reactivity of metal oxide precursors towards a specific solvent complicates the synthesis of oxides containing two or more metals. In organic solvents it is easier to match the reactivity of the metal oxide precursors and of the dopants in comparison to aqueous systems, which is crucial for obtaining phase pure products.

This article is divided into several sections. In the first part we give a short overview of nonaqueous surfactant-free sol–gel routes, including a presentation of ternary metal oxide nanoparticles synthesized by these methodologies and some general mechanistic principles regarding the chemical pathways leading to oxidic nanoparticles, followed by the morphology-controlled preparation of lanthanum hydroxide nanoparticles as an example that shows that also organic species formed *in situ* during the reaction course may play a crucial role in determining the crystal shape. Anisotropic crystallite growth can be induced by organic species that are not initially present in the reaction mixture, but formed *in situ*, and therefore the study of all the organics in nonaqueous reaction systems is a prerequisite on the way to completely understand the formation of nanoparticles on a molecular level. The third section reports on manganese oxide nanoparticles with an unusual superstructure exhibiting superparamagnetism. This example nicely illustrates how the structural and physical properties of nanoparticles can differ from the corresponding bulk material. Finally, doping of titania nanoparticles with transition metal ions and their magnetic properties is described.

2. Experimental details

2.1. Materials

Titanium tetrachloride (99.995+ %), titanium tetraisopropoxide (99.999%), iron(III) acetylacetonate (99.9+ %), cobalt(II) acetylacetonate (97%), anhydrous benzyl alcohol (99.8%), and 2-butanone (99+ % spectrophotometric grade) were obtained from Aldrich and used without further purification. The solvothermal treatment was performed in Parr acid digestion bombs with 45 ml Teflon cups.

2.2. Synthesis

All synthesis procedures were started under argon atmosphere in a glovebox. The experimental details for obtaining manganese oxide and lanthanum hydroxide nanoparticles are described in Refs. [15,16], respectively. 3 mol% Co/Fe-doped titania samples were prepared by mixing the corresponding Co/Fe precursor [$Co(acac)_2$/$Fe(acac)_3$] with either 0.5 ml of $Ti(OiPr)_4$ or 0.5 ml of $TiCl_4$. This mixture was then dissolved in 20 ml of the organic solvents: benzyl alcohol, 2-butanone, or a 1:1 vol. mixture thereof (10 ml benzyl alcohol and 10 ml 2-butanone). The mixing of the precursors with the solvent was directly performed in the 45 ml Teflon cups of the acid digestion bombs. The autoclave was taken out of the glovebox and heated in a furnace at 200 °C for 3 days. The resulting suspensions were centrifuged to separate the precipitate from the mother liquid. Excess organic impurities were removed by repeated washing steps in 10 ml of high-grade purity ethanol and subsequently dried in air at 60 °C.

2.3. Characterization

X-ray powder diffraction (XRD) patterns were measured in reflection mode with Cu$K\alpha$ radiation on a X'Pert PRO diffractometer (PANalytical manufacturer) equipped with a X'Celerator detector. The instrumental contribution to the peak broadening caused by instrumental aberrations was removed by the deconvolution method with highly crystalline NIST SRM 660a LaB_6 powdered sample as a standard. The analysis of the XRD patterns was done following a well-established Rietveld procedure using the program FULLPROF [17]. Transmission electron microscopy (TEM) measurements were performed on a Zeiss EM 912Ω instrument at an acceleration voltage of 120 kV, while high-resolution transmission electron microscopy (HRTEM) characterization together with energy-dispersive X-ray spectroscopy (EDX) was done using a Philips CM200-FEG microscope (200 kV, $Cs = 1.35$ mm). For TEM characterization, one drop of the dispersion in ethanol from the last washing step was released onto a copper grid covered by an amorphous carbon film. To restrict the agglomeration of the nanoparticles during drying, the copper grid was placed on a filter paper. Analytical ultracentrifugation (AUC) was performed with a Beckman Optima XL-I centrifuge (Beckman/Coulter) with a scanning absorption optics and online Rayleigh interferometer. The magnetization at applied field was measured with a commercial Quantum Design SQUID magnetometer, equipped with a 5 T superconducting magnet. The temperature dependence of the DC susceptibility was measured while cooling the sample from 300 down to 2 K in a magnetic field of 1000 Oe. For the magnetization measurements the samples were loaded into a gelatin capsule and the measurements were corrected for the diamagnetic contribution of the sample holder.

3. Results and discussion

3.1. Short overview of nonaqueous and surfactant-free routes to metal oxide nanoparticles

Nonaqueous and surfactant-free sol–gel routes are based on the chemical transformation of molecular metal oxide precursors such as metal halides, alkoxides, acetates, or acetylacetonates into an extended metal oxide network in various organic solvents such as alcohols, amines, aldehydes, or ketones under exclusion of water. These procedures gave access to a wide variety of binary, ternary, and doped metal oxide nanoparticles with crystallite shapes ranging from spheres to rods and wires. A rather exhaustive list of metal oxides synthesized by these routes can be found somewhere else [13]. However, in here we will just briefly discuss the preparation of selected ternary metal oxide nanoparticles that are particularly difficult to obtain by other synthesis routes on that size scale. Indium tin oxide was prepared from indium acetylacetonate and tin *tert*-butoxide in benzyl alcohol at 200 °C [18]. The choice of two chemically different precursors is crucial for obtaining the solid solution rather than the two individual binary phases In_2O_3 and SnO_2. Obviously the chemical reactivity of these two precursors towards benzyl alcohol is a perfect match with respect to the condensation reactions leading to the formation of the ternary metal oxide network. The nanoparticles are crystalline with diameters ranging from 5 to 10 nm (Fig. 1(a)). The synthesis of $BaTiO_3$ involved the reaction of metallic barium with benzyl alcohol (leading to Ba^{2+}, benzyl alcoholate, and hydrogen gas), followed by the addition of titanium isopropoxide and subsequent solvothermal treatment at 200 °C [19]. The resulting nanoparticles exhibited sizes in the range of 4–8 nm (Fig. 1(b)) with a complex crystal structure, which was cube-like in general; however, showed locally some slight distortions [20]. Luminescent colloidal $ZnGa_2O_4$ nanoparticles with narrow size distribution from 6 to 8 nm were obtained from zinc and gallium acetylacetonate in benzylamine at 200 °C (Fig. 1(c)) [21]. Other complex metal oxide nanoparticles synthesized by nonaqueous and surfactant-free sol–gel routes include $YNbO_4$ (from niobium chloride and yttrium acetylacetonate hydrate in benzyl alcohol, Fig. 1(d)) [22], $NaTaO_3$ (from sodium and tantalum ethoxide in benzyl alcohol, Fig. 1(e)) [23], and $BaSnO_3$ (from metallic barium and tin *tert*-butoxide in 2-butanone, Fig. 1(f)) [23].

In aqueous sol–gel chemistry water acts as oxygen source for the formation of the metal oxide species. In the case of nonaqueous sol–gel processes, where intrinsically no water is present, two main questions arise: (i) where is the oxygen come from and (ii) how is it transferred from the source to the metal centre? One possibility to answer this question is the identification and quantification of the organic by-products at the end of the synthesis procedure [11]. It turned out that it is possible to correlate the organic side reactions with the formation of the inorganic nanoparticles, providing unique mechanistic insights into the chemical pathways [11]. For example, the reaction between titanium tetrachloride and benzyl alcohol led to anatase nanoparticles and benzyl chloride, which is characteristic for a condensation reaction based on alkyl halide elimination (Scheme 1a). The reaction of hafnium ethoxide in benzyl alcohol yielded HfO_2 and organic ethers, which is typical for ether elimination processes (Scheme 1b). If a metal acetate is reacted with an alcohol, like in the case of zinc acetate and benzyl alcohol, ester elimination (benzyl acetate in this example) is responsible for the formation of the metal oxide framework (Scheme 1c). Ketones as solvents undergo aldol condensation reactions under elimination of water and formation of α,β-unsaturated carbonyl compounds. An example along these lines is the formation of anatase nanoparticles starting from titanium isopropoxide and acetone (Scheme 1d). An interesting reaction mechanism was found in the case of $BaTiO_3$, CeO_2, and Nb_2O_5, whose formation involved a C–C coupling mechanism between the benzylic carbon atom of benzyl alcohol and a β-carbon atom of the alkoxide ligand of the precursor molecule. Scheme 1e shows the reaction between niobium ethoxide and benzyl alcohol, resulting in Nb_2O_5 and 3-phenylpropanol. It is interesting to note that in spite of the large number of possible precursor–solvent combinations, most of the nonaqueous sol–gel processes can be described by these five different condensation reactions. On the other hand, one has to keep in mind that the study of the condensation reactions provides only information about the chemical pathways, but does not offer any answers concerning the relationship between a particular synthesis system and the particle morphology. It is obvious that the organic species strongly influence the structural,

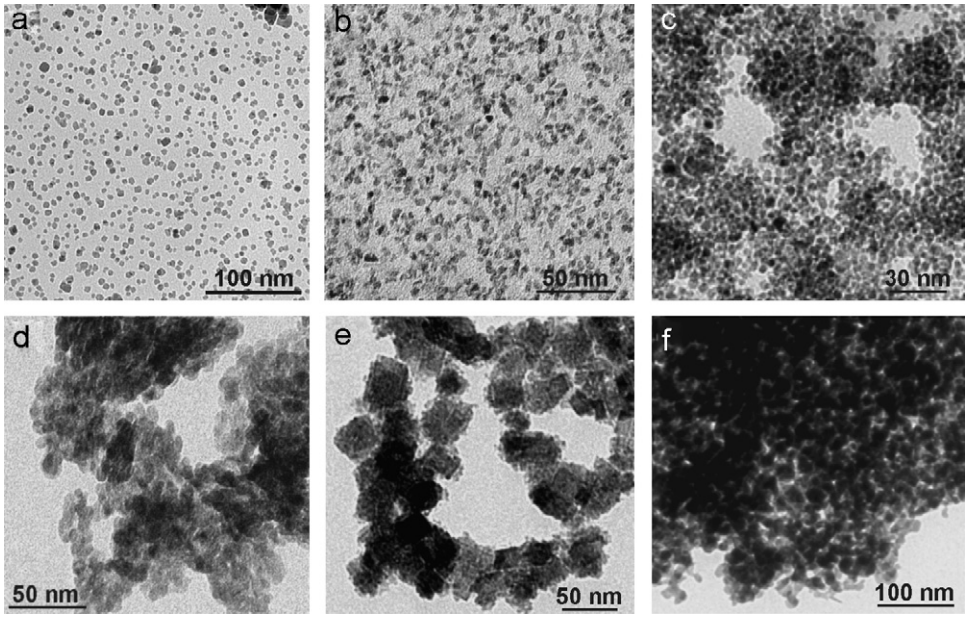

Fig. 1. TEM overview images of (a) indium tin oxide, (b) $BaTiO_3$, (c) $ZnGa_2O_4$, (d) $YNbO_4$, (e) $NaTaO_3$, and (f) $BaSnO_3$ nanoparticles.

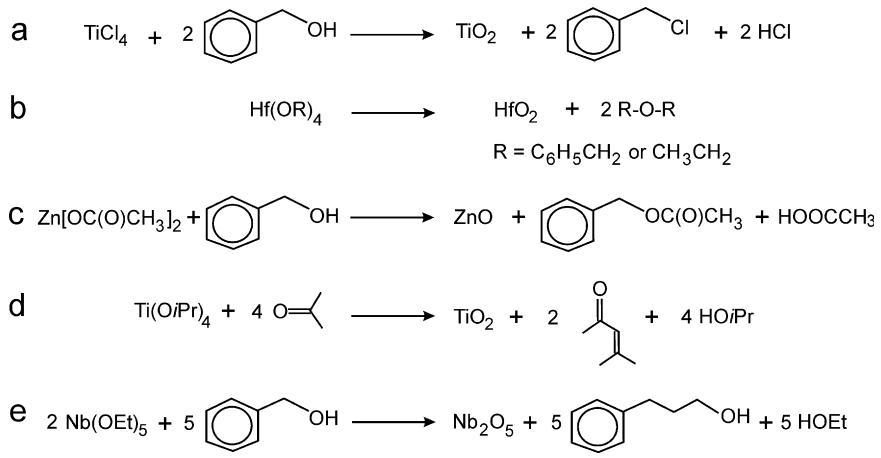

Scheme 1. Selected examples of condensation steps leading to the formation of the metal oxide nanoparticles and the corresponding organic species: (a) alkyl halide elimination, (b) ether elimination, (c) ester elimination, (d) aldol condensation, and (e) C–C bond formation.

compositional and morphological characteristics of the inorganic product, however, it remains an open question, how this occurs on a molecular level.

3.2. Lanthanum hydroxide nanoparticles: anisotropic system with controlled morphology

The design of one-dimensional nanostructures is interesting due to the restriction of carrier motion in two directions, which consequently results in different electron-transport properties compared to the corresponding bulk material [24]. The lanthanum hydroxide nanoparticles were synthesized with a nonaqueous sol–gel process involving the reaction of La(O*i*Pr)$_3$ and $KMnO_4$ with benzyl alcohol, 2-butanone and 1:1 vol. mixture thereof. The interesting feature is that the particle shape and size ranging from long nanofibers with an average aspect ratio of 60 (Figs. 2(a) and (b)) to short nanorods with an average aspect ratio of 2.6 (Figs. 2(g) and (h)), depends strongly on the molar La(O*i*Pr)$_3$-to-$KMnO_4$ ratio, so that the adjustment of this parameter allows the control of the $La(OH)_3$ morphology [16]. $KMnO_4$ can be therefore regarded as an indirect structure directing agent, since the acicular shape of $La(OH)_3$ nanoparticles is induced by the complexation of benzoate species (formed upon oxidation of benzyl alcohol by permanganate) selectively to all crystal faces except the {001} facet. The second important role of $KMnO_4$ is in the control of phase purity (composition) of the final compound. When the La(O*i*Pr)$_3$-to-$KMnO_4$ ratio is 1:1 in the 1:1 vol. mixture of benzyl alcohol and 2-butanone, the detected minor phase is β-MnOOH (Feitknechtite). Phase purity is achieved only in the case of 1:0.5 precursors ratio. Further decrease of $KMnO_4$ leads to the formation of $LaCO_3OH$ as by-product. HRTEM analysis of the sample with the highest $KMnO_4$ content is presented in this paper and shown in Fig. 2(d). As one can clearly see the $La(OH)_3$ nanofiber consists of two single-crystals marked with A and B in the image. The corresponding power spectrum shown in the inset indicates bicrystalline features, since the spots denoted by arrowheads look elongated, i.e., they belong to different crystals. To elucidate the orientation relationship between the two crystals, separate Fourier analysis of crystals A and B was performed and the results are displayed in Figs. 2(e) for crystal A and (f) for crystal B. According to that the following orientation relationship can be established: $[1\bar{1}\bar{1}]_A||[010]_B$ and $[1\bar{1}2]_A||[001]_B$. The absence of a common zone-axis indicates that the single-crystal A can not be related to the single-crystal B by a simple rotation around the common zone-axis, but one should also include a tilting of the crystal. Such a complex orientation relationship gives interesting insight into the crystallization and growth process, and points to a nucleation and attachment process often observed for anisotropic nanostructures [25–29]. The cross-sectional TEM image recorded perpendicular to the nanofiber axis, shown in Fig. 2(c), presents faceted and non-faceted cross sections. Non-faceted ones have the finite rectangular shape confirming the proposed nanofiber morphology. Additional faceted shapes in the form of regular hexagon corroborate that their growth direction is really [001], although this cannot be regarded as the unique growth direction.

3.3. Manganese oxide nanoparticles: superstructure and superparamagnetism

The synthesis of manganese oxide nanoparticles (MnO and Mn_3O_4) constitutes an illustrative case as to how the simple benzyl alcohol route generates rather peculiar structural features like Mn vacancy-induced superstructure at the level of nanoparticles. The reaction of manganese(II) acetylacetonate with benzyl alcohol yielded 80 wt% MnO (manganosite) and 20 wt% Mn_3O_4 (hausmannite) in the form of nanoparticles, whereas the replacement of manganese(II) acetylacetonate with $KMnO_4$ resulted in a nanoparticulate material with 87 wt% of Mn_3O_4 and 13 wt% of MnO [15]. The obtained MnO nanoparticles (MnO-dominated product) are single-crystalline and exhibit a rather uniform shape with nanoplatelets as the main species (Fig. 3(a)). The particle diameters are in the range from 12 to 88 nm with an average value of 37 nm. On the other hand, Mn_3O_4 nanoparticles (Mn_3O_4-dominated sample) appear with various morphologies including plate-like shapes, spherules, ellipsoids, cubes, and rhombohedra, having a size distribution in the range from 15 to 69 nm with an average value of 32 nm. The microstructural investigation of the MnO nanoparticles revealed the existence of a superstructure, which was detected by HRTEM and SAED at many different spots of several nanoparticles. One of such spots (HRTEM image) was chosen for the inclusion in this review, and it is displayed in Fig. 3(b). The corresponding Fourier-filtered image presented in Fig. 3(c) intelligibly shows arrays of fringes, i.e., one bright line (denoted by arrowheads) alternates with a less bright one. The distance between two bright lines is exactly the double of the distance between a bright-less bright one. The power spectrum taken from Fig. 3(b) and shown in (e) exhibits spots which can be indexed only with the rational Miller indices 0.5 0.5 0.5 as shown for the spot marked with the white arrowhead. Moreover, an electron diffraction pattern (Fig. 3(d)) taken from the same nanoparticle has the configuration of Laue spots characteristic

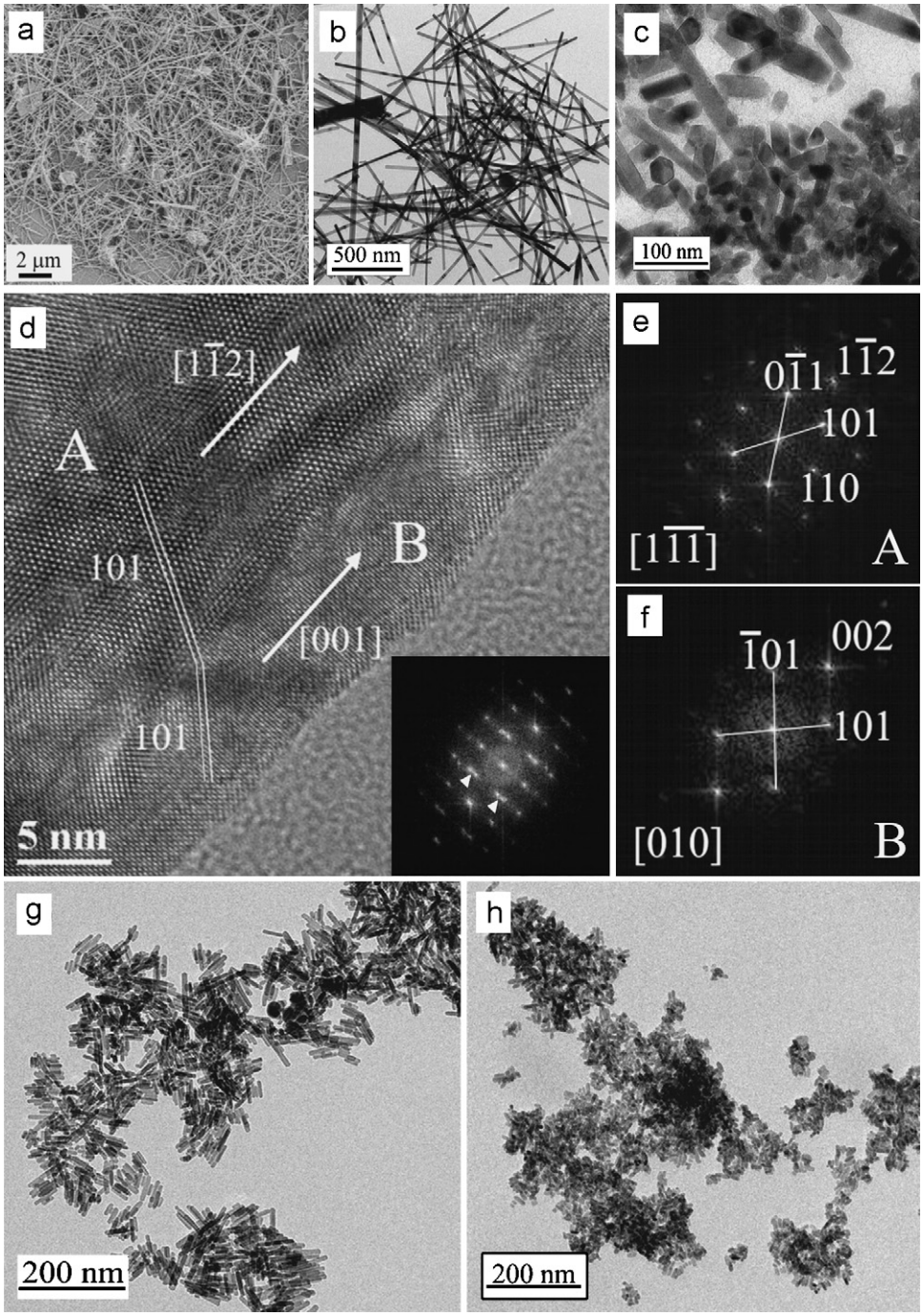

Fig. 2. (a) SEM image of the $La(OH)_3$ nanofibers synthesized from $La(OiPr)_3$ and $KMnO_4$ in the molar ratio 1:1 and equivolume mixture of benzyl alcohol and 2-butanone, (b) TEM image of the sample described in (a), (c) corresponding cross-sectional TEM image, (d) HRTEM image of a part of a $La(OH)_3$ nanofiber of the system in (a) with its power spectrum as inset, (e) power spectrum of the crystallite marked with A in (d), (f) power spectrum of the crystallite marked with B in (d), (g) and (h) representative TEM images of the samples synthesized from $La(OiPr)_3$ and $KMnO_4$ in the ratio 1:0.25 (g), and 1:0 (h) with the same combination of solvents as in (a).

for the [$\bar{1}$ 1 0] zone-axis orientation with the superlattice reflection 0.5 0.5 0.5, denoted with a black arrowhead. All these evidences indicate the presence of a superstructure, which is formed by the regular distribution of Mn vacancies in the MnO crystal matrix. The atomic model of such a cubic superstructure is shown in Fig. 3(f), and the unit cell (supercell) is outlined with a white rectangle. The superstructure is generated rather simple by the removal of Mn atoms from the corners and centers of the faces in a doubled unit cell of MnO. The calculated formula of such Mn vacancies ordered superstructure is $Mn_{0.875}O_x$ [15]. Based on the superstructural model, HRTEM image simulation of the crystal in the [$\bar{1}$10] zone-axis was performed and the resulting image (inset in Fig. 3(c)) nicely matches with the corresponding experimental HRTEM image given in Fig. 3(c). Concerning the magnetic properties, zero-field cooled magnetic susceptibilities of MnO nanoparticles show a clear maximum at low temperatures. The temperature, where this maximum occurs, is strongly field dependent, ranging from 29 K at the field of 100 Oe to 19 K at 10 kOe. Such an observed field dependence of the blocking temperature is a typical signature of superparamagnetic (monodomain) particles. This finding is rather surprising, since in the literature it was reported that nanocrystalline MnO is

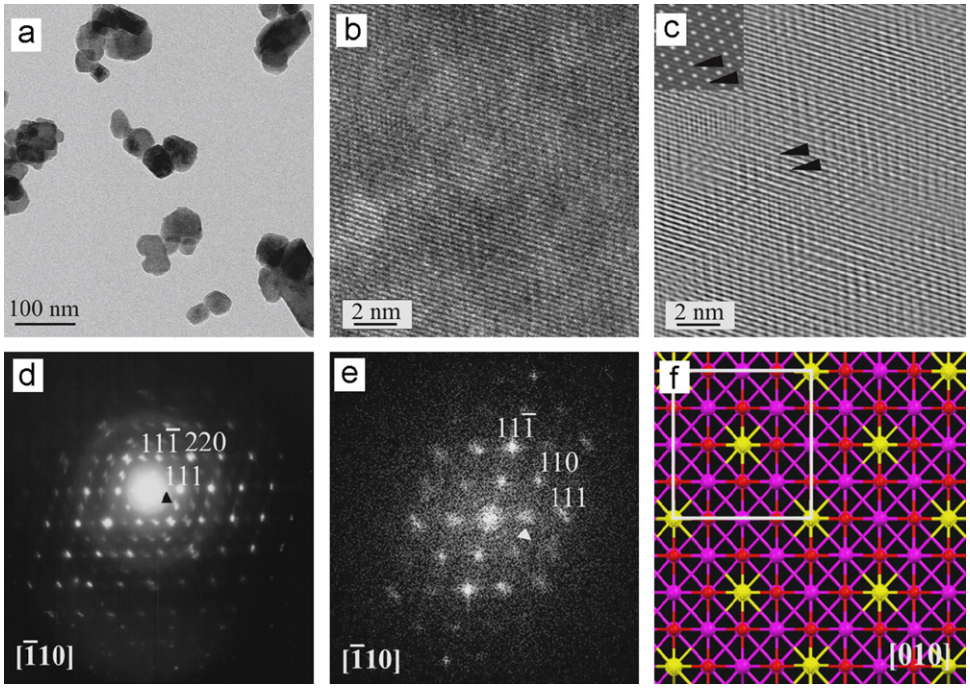

Fig. 3. (a) TEM overview of MnO nanoparticles, (b) HRTEM image of a part of a single-crystalline MnO nanoparticle, (c) Fourier-filtered image of the HRTEM image in (b). Arrows denote the lattice fringes corresponding to the superstrucure. Simulated image based on the structural model shown in (f) is displayed in the inset, (d) corresponding SAED pattern with the two principal reflections (111,11$\bar{1}$) as well as their sum (220). The arrowheads in (d) and (e) denote the superlattice reflection (0.50.50.5), (e) power spectrum of part (b), (f) atomic model of the $Mn_{0.875}O_x$ superstructure viewed along [010] (manganese atoms, purple; oxygen atoms, red; Mn vacancies, yellow). The image (f) is reproduced from Ref. [15]. Copyright 2007 American Chemical Society.

ferromagnetic, although its bulk counterpart is antiferromagnetic [30,31]. The origin of the superparamagnetic-like behavior, which is frequently observed in nanoparticles, can be explained either by the sudden change of the antiferromagnetic into ferromagnetic interactions due to the more deformed structure or by uncompensated surface spins.

3.4. *Fe- and Co-doped titanium dioxide*

Diluted magnetic semiconductors (DMS) with TiO_2 as a possible host has received significant attention, especially Co-doped TiO_2 with anatase [32] and rutile structure [33], and Fe-doped TiO_2 (anatase) [34,35]. The design of such ferromagnetic DMS's with Curie temperature above room temperature is essential for applications in spintronics. The manifestation of ferromagnetism in DMS's is not straightforward. The key factor in activation of ferromagnetism is to introduce interaction between the magnetic atoms (Co, Fe). Investigating Co^{2+}- and Cr^{3+}-doped TiO_2, Bryan et al. [36] have found that the most important factor for activating ferromagnetism is the creation of oxygen vacancies at nanocrystal fusion interfaces. Focusing on Fe and Co as dopants, depending on the synthesis procedure as well as on the dimensionality of the produced system, various magnetic states were found (paramagnetic, ferromagnetic) [32,36–41]. Here we present a short study concerning the nonaqueous synthesis, characterization, and investigation of the magnetic properties of Co- and Fe-doped TiO_2 nanoparticles. The reaction between either $TiCl_4$ or Ti(O*i*Pr)$_4$ and benzyl alcohol or 2-butanone results in the formation of phase pure TiO_2-anatase nanoparticles. Benzyl alcohol has already been found to be an excellent reaction medium for the preparation of doped metal oxides such as Mn- and Co-doped ZnO, or Mn-doped ZrO_2 [42,43]. The color of the resulting titania powder is white, however upon doping it is clearly changed in a rather complex way: dark green in the case of cobalt doping using Ti(O*i*Pr)$_4$ as a titania precursor, or light brown

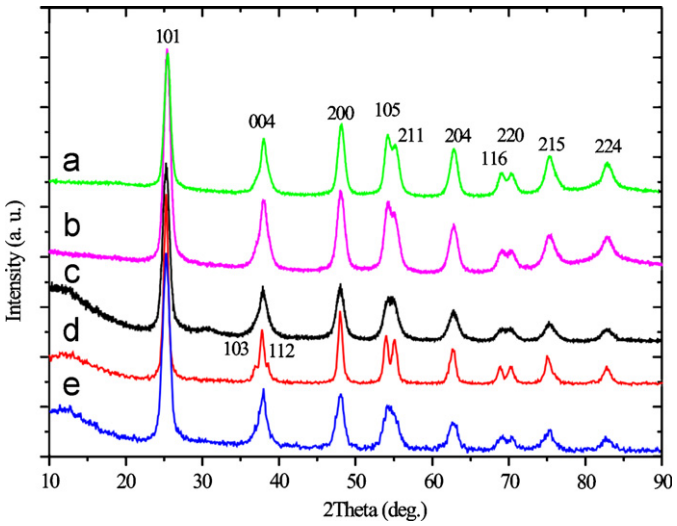

Fig. 4. XRD patterns of the investigated doped titania samples in various solvents (benzyl alcohol (BA), 2-butanone (BUT) and a mixture thereof) and precursors (Ti(O*i*Pr)$_4$, $TiCl_4$). (a) Fe-doped TiO_2 (BA, Ti(O*i*Pr)$_4$), (b) Fe-doped TiO_2 (BA+BUT, Ti(O*i*Pr)$_4$), (c) Fe-doped TiO_2 (BUT, Ti(O*i*Pr)$_4$), (d) Co-doped TiO_2 (BA+BUT, $TiCl_4$), and (e) Co-doped TiO_2 (BA+BUT, Ti(O*i*Pr)$_4$). The Miller indices of the anatase TiO_2 are denoted.

starting from $TiCl_4$. In the case of iron doping for both titania precursors, the resulting powders are light brownish. All samples were investigated by XRD as a primary tool for phase identification, detection of eventual crystalline impurities and an estimate of the average crystallite size. The XRD patterns of the investigated doped titania samples are displayed in Fig. 4. The structural and microstructural information is extracted by processing the corresponding XRD patterns with the Rietveld method. For all examined samples, the observed reflections are indexed based on

tetragonal anatase TiO_2 with the space group $I4_1/amd$ (ICDD PDF no. 21-1272). According to XRD or at least up to the detection limit of XRD, impurity peaks, which might be attributed to the presence of a crystalline by-product, were not detected, confirming the phase purity of the final products. As one can observe from Fig. 4, there is not a big difference in the profile features among the TiO_2 XRD patterns corresponding to the different solvent–precursor mixtures. However, careful inspection of the XRD profiles, particularly on the group of the reflections 1 0 3, 0 0 4, and 1 1 2, one can see that these reflections are better resolved only in Co-doped titania prepared from $TiCl_4$ (Fig. 4(d)). Consequently, the average crystallite size estimated from the peak broadening gives a larger value of 11.6 nm for the Co-doped TiO_2 synthesized from $TiCl_4$, while in all other cases independently from the dopant, the average crystallite size is below 10 nm. More precisely, for Fe-doped TiO_2 prepared by mixing $Ti(OiPr)_4$ and 2-butanone or for Co-doped TiO_2 ($Ti(OiPr)_4$ in isovolume mixture of benzyl alcohol and 2-butanone) it amounts to 6.8 nm, whereas its value is 7.4 nm for the Fe-doped TiO_2 synthesized by mixing $Ti(OiPr)_4$ and benzyl alcohol. The main parameter, which mostly influences the

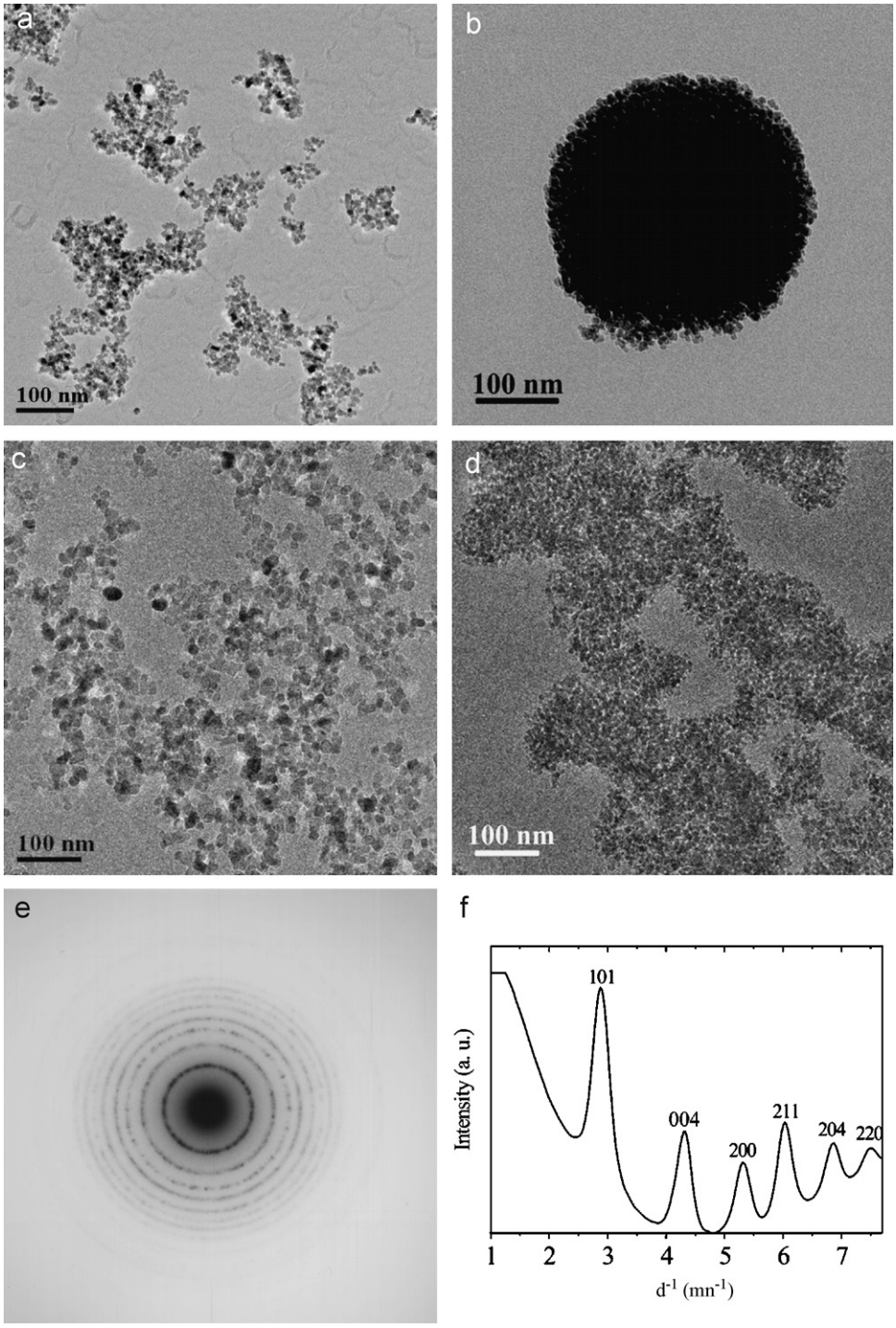

Fig. 5. TEM images of the Fe (a, b), and Co (c, d)-doped titanium dioxide nanoparticles obtained in (a) titanium tetraisopropoxide-benzyl alcohol, (b) titanium tetraisopropoxide-2-butanone, (c) titanium tetrachloride–benzyl alcohol+2-butanone, (d) titanium tetraisopropoxide–benzyl alcohol+2-butanone, (e) selected SAED pattern of the Co-doped TiO_2 displayed in (d), (f) corresponding radial intensity distribution of (e).

size of the final TiO_2 nanoparticles, is thus the titanium oxide source $TiCl_4$ or $Ti(OiPr)_4$.

The morphology and the qualitative degree of agglomeration/dispersibility of the doped titania nanoparticles was studied by TEM. Figs. 5(a)–(d) provide representative TEM overview images of the doped TiO_2 nanoparticles prepared under various conditions. Concerning dispersibility, the highest degree of agglomeration is noticed for 2-butanone as solvent (Fig. 5(b)). A bit lower degree of agglomeration is observed in the case of the equivolume mixture of benzyl alcohol and 2-butanone and $Ti(OiPr)_4$ as a titanium dioxide precursor (Fig. 5(d)). Improved dispersibility is achieved by using pure benzyl alcohol as the solvent (Fig. 5(a)), however, $TiCl_4$ and the combination of benzyl alcohol and 2-butanone gave the best dispersibility of nanoparticles (Fig. 5(c)). TEM study of cobalt and iron-doped titania nanoparticles evidenced that the degree of agglomeration is independent of the dopant type. It is mainly influenced by the solvent and the titanium dioxide precursor. In all studied reaction systems, the obtained titanium dioxide nanoparticles exhibit basically the same shape. The particles are mostly spherical with diameters in the range of 4–14 nm with an average value of 8.5 nm for the systems $Ti(OiPr)_4$–benzyl alcohol and $Ti(OiPr)_4$–benzyl alcohol+2-butanone. Switching from $Ti(OiPr)_4$ to $TiCl_4$ and keeping the same combination of solvents, the range of particle diameters is increased to 7–25 nm with the average at 14 nm. Accordingly, the TEM findings nicely confirm the peak broadening analysis of the XRD powder patterns. The particle size distribution of the Fe-doped titania prepared from the solution of $TiCl_4$ and the mixture of benzyl alcohol and 2-butanone was measured by AUC, which offers the possibility to directly determine the size distribution of the nanoparticles in liquid phase (here ethanol) with good statistics [44]. One should emphasize that the extracted particle size represents the hydrodynamic radius, which means that their values are slightly higher than the ones corresponding to the purely inorganic core. The AUC result for the Fe-doped TiO_2 is displayed in Fig. 6. The particles show a bimodal size distribution in the range between 6 and 46 nm with two maxima at around 15 and 20 nm. Obviously, in addition to individual, completely isolated nanocrystals, also small agglomerates are present. Nevertheless, the degree of agglomeration of these nanoparticles in solution is still relatively small.

Further studies regarding phase purity and crystallinity were done using the SAED technique. Fig. 5(e) depicts an SAED pattern of Fe-doped TiO_2 prepared by mixing $Ti(OiPr)_4$ and benzyl alcohol. The Debye–Scherrer rings clearly indicate the polycrystalline nature of the powder. The corresponding radial intensity diagram in Fig. 5(f) perfectly matches the corresponding XRD pattern (Fig. 4(a)) and illustrates that the tetragonal anatase structure is the only crystal structure existing in the sample. Moreover, SAED analysis of all investigated Co- and Fe-doped titania samples did not reveal the existence of any impurity in crystalline form which might arise due to the doping. Therefore, crystalline compounds like cobalt or iron oxides as well as the metallic form of these metals were not detected by XRD or by SAED.

Energy-dispersive X-ray analysis (EDX) was used to determine the elemental composition of the nanoparticles, mainly to confirm the presence of the dopant atoms within the titania nanoparticles and to calculate the effective dopant concentration. Fig. 7 shows selected EDX spectra taken from one representative Co-doped TiO_2 prepared from $Ti(OiPr)_4$ as titania precursor, and another representative Fe-doped TiO_2 sample ($TiCl_4$ as precursor). In addition to titanium, cobalt, and oxygen as main species, also carbon and copper (from the TEM grid) were detected. The concentration of Co equals to 1.1 at% (or 2.4 wt%), whereas Fe interestingly was not detected at all. The amount of cobalt found in the sample is obviously less than the initial concentration, which indicates that the doping efficiency is less than 100%. This result is also confirmed by the magnetic measurements (see below).

Further investigation of the structure with the focus on the crystallinity of the doped titania nanoparticles was achieved by HRTEM. Figs. 8(a) and (c) show representative HRTEM images of iron- and cobalt-doped titania nanoparticles prepared by introducing $TiCl_4$ either in benzyl alcohol (in the case of iron as dopant) or in the mixture of benzyl alcohol and 2-butanone (cobalt case), respectively. Particularly, Fig. 8(a) displays well-resolved lattice fringes pointing to the high crystallinity of the obtained samples. All *d*-spacings of the lattice fringes correspond to the reflection list of anatase, which is in accordance with the XRD results. An interesting feature is the appearance of well-faceted anatase crystals that are in Fig. 8(a) outlined for better visibility. The same finding is also reported in Fig. 8(c), where an isolated single-crystalline cobalt-doped TiO_2 nanoparticle is presented. Its single-crystallinity is corroborated with the corresponding power spectrum (Fig. 8(d)), which consists of an array of discrete spots. Each spot is according to its position unambiguously assignable to

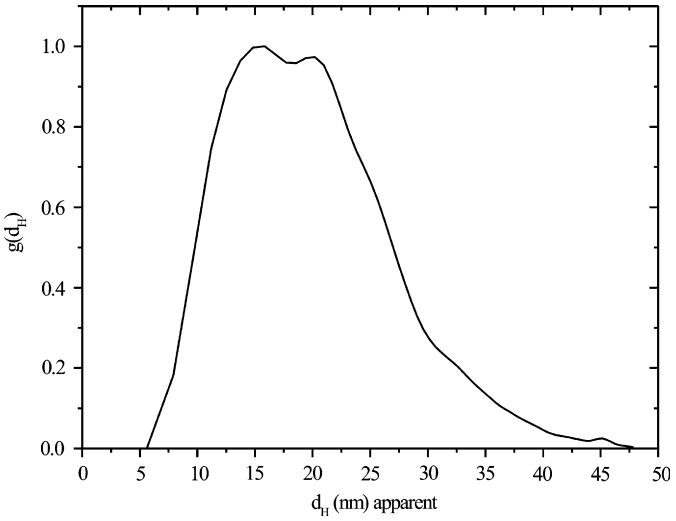

Fig. 6. Particle size distribution of Fe-doped TiO_2 synthesized from titanium tetrachloride and a mixture of benzyl alcohol and 2-butanone extracted by analytical ultracentrifugation (AUC) of the particles in ethanol.

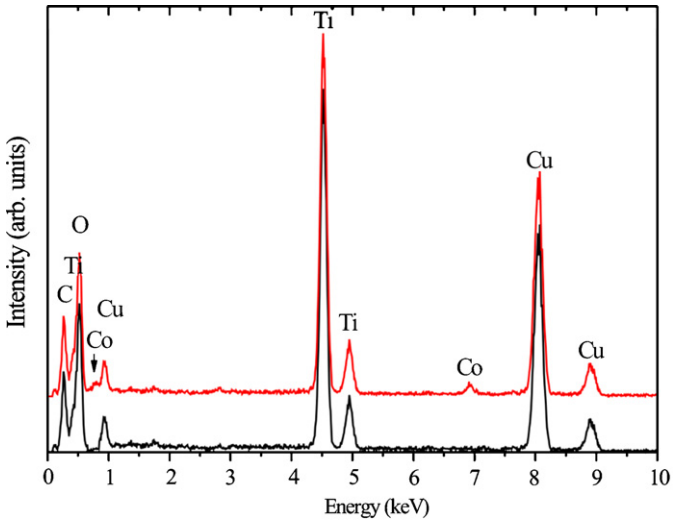

Fig. 7. Some EDX spectra of the investigated doped TiO_2 samples. Upper spectrum: 3% Co:TiO_2. Lower spectrum: 3% Fe:TiO_2.

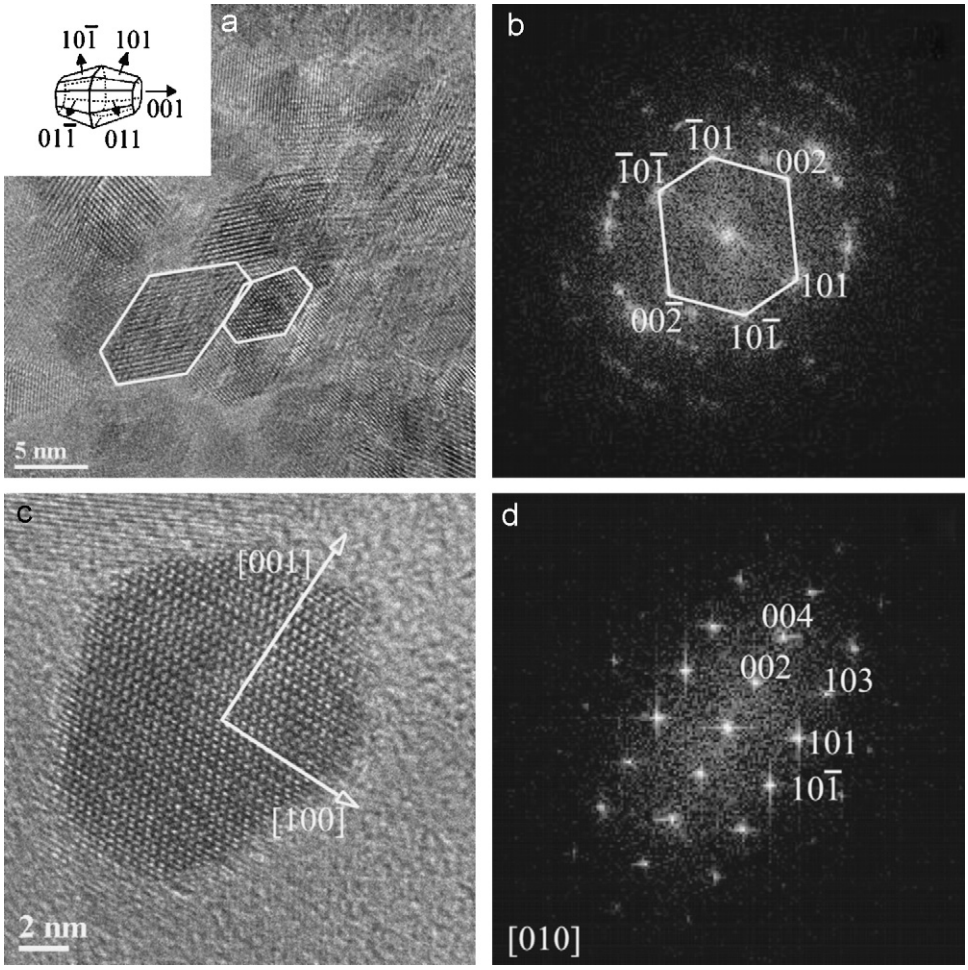

Fig. 8. (a) HRTEM image of the iron-doped titania nanoparticles synthesized by mixing $TiCl_4$ and benzyl alcohol, (b) corresponding power spectrum of (a), (c) HRTEM image of an isolated single-crystal nanoparticle of cobalt-doped titania prepared from $TiCl_4$ and a mixture of benzyl alcohol and 2-butanone, and its power spectrum (d). Inset in figure (a) shows the model of well-faceted TiO_2 nanoparticles from (a) and (c).

the corresponding anatase *hkl* reflection; some of them are indexed in Fig. 8(d). The analysis of the power spectrum indicates that the isolated titania nanocrystal is oriented along the [010] direction with respect to the electron beam. The observed faceted crystals are in the form of a hexagon truncated with two {001} and four {101} faces. Such a hexagonal shape in the [010] projection of a truncated octagonal bipyramid is sketched in the inset of Fig. 8(a). The truncated octagonal bipyramid is terminated by two equivalent {001} faces with high-surface energy and eight equivalent {101} faces with relatively low surface energy [45]. Natural anatase crystals predominantly expose the {101} planes, indicating that these planes have the lowest surface energy [46]. It has been shown that anatase nucleates as truncated octagonal bipyramid seeds, which further grow and combine to the final anatase crystal [47]. The final shape of the anatase nanocrystal is therefore a result of the competition between the relative surface energies of the {001} and {101} faces. It is noteworthy that in the case of undoped TiO_2 synthesized in the same way as the doped ones, the faceted anatase nanocrystals were not observed at all. This observation implies that the dopants probably catalyze the formation of coordinating organic species [11] that influence the growth rates of the different crystal faces, as found for selectively coordinating surfactants [45].

The HRTEM image shown in Fig. 8(a) and its corresponding power spectrum (Fig. 8(b)) indicate that the outlined faceted anatase nanocrystals are in some kind of oriented attachment relationship. The irregular hexagon displayed in Fig. 8(b) reveals that the outlined faceted anatase nanocrystals have the {101} crystallographic plane in common and their long axes are parallel. This is rather unusual, since the attachment of anatase nanocrystals typically occurs on high-surface-energy planes such as {112} or {001} [48,49], however, sometimes also along the [010] direction [50].

The magnetic properties of the Fe-doped TiO_2 nanoparticles synthesized from $Ti(OiPr)_4$ in benzyl alcohol were investigated. The temperature dependence of the magnetic susceptibility (measured at 1000 Oe and displayed in Fig. 9(a)) has a typical paramagnetic shape, and adheres to the Curie–Weiss law: $\chi(T) = \chi_0 + C/(T-\theta)$, where χ_0 is a temperature-independent susceptibility, C is the Curie constant, and θ is the asymptotic Curie–Weiss temperature. The temperature-independent susceptibility is composed of Van Vleck paramagnetism, and Larmor diamagnetism of the core electrons. Fitting the Curie–Weiss law to the susceptibility data we obtain $\chi_0 = 9.25 \times 10^{-7}$ emu/g, $C = 3.69 \times 10^{-4}$ emuK/g, and $\theta = -1.17$ K. The Curie constant C is further described as

$$C = N\mu_{\text{eff}}^2/(3k_B), \quad (1)$$

where N is the number of magnetic atoms per unit volume, μ_{eff} is the effective moment per atom, and k_B is the Boltzmann constant. Assuming that the Curie constant C is only due to the iron, and supposing that the oxidation state of the iron cation is 3+, we can estimate the iron concentration in the sample. In the calculation a value of $\mu_{\text{eff}} = 5.92\mu_B$ per Fe atom is suitable for Fe^{3+}

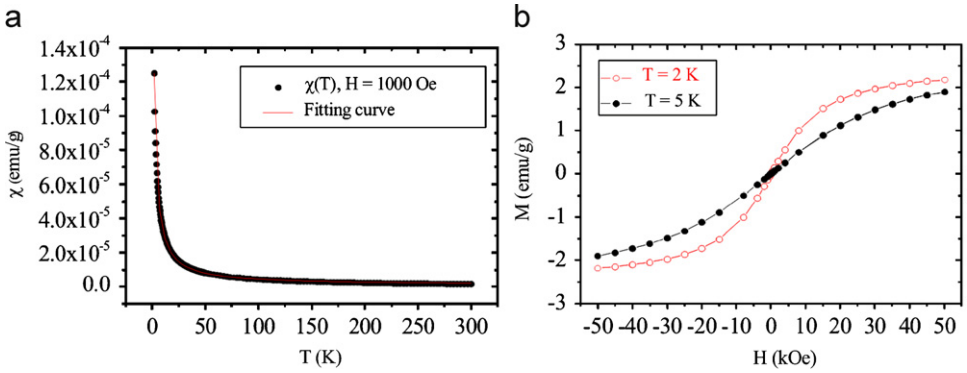

Fig. 9. (a) Temperature dependence of magnetic susceptibility χ measured in DC field $H = 1000$ Oe for 3% Fe-doped TiO_2 synthesized from $TiCl_4$ and a mixture of benzyl alcohol and 2-butanone. The red curve is the fit to the data using the Curie–Weiss law, (b) magnetization-field curves taken at 2 and 5 K.

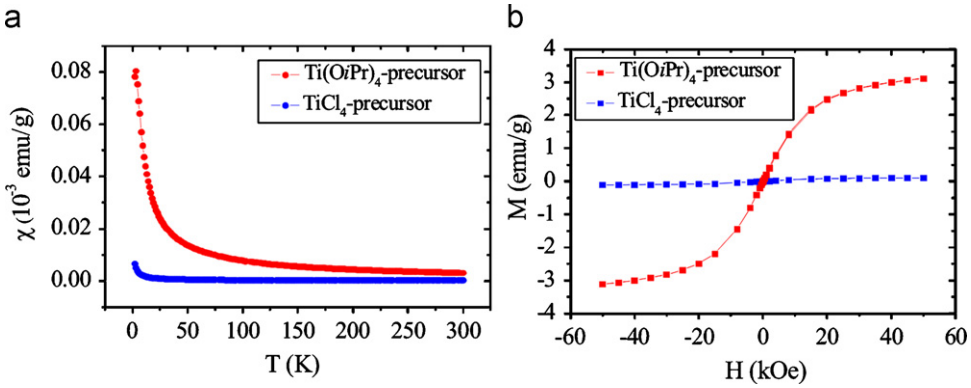

Fig. 10. (a) Temperature dependence of magnetic susceptibility χ measured in DC field $H = 1000$ Oe for 3% Co-doped TiO_2 samples synthesized from $TiCl_4$ (blue curve) and $Ti(OiPr)_4$ (red curve) in a mixture of benzyl alcohol and 2-butanone, (b) magnetization-field curves taken at 2 K.

ions, and using Eq. (1) the iron concentration was found to be 0.45 wt% or 0.22 at%. Such a low concentration of iron atoms in the titania matrix explains the absence of their lines in the EDX spectrum, because the detection limit of the EDX detector is around 0.1 wt%, which is close to the real iron content. The magnetization $M(H)$ as a function of the magnetic field for the same sample is measured in the low-temperature regime and shown in Fig. 9(b). The magnetization curves measured at 2 and 5 K are reversible and can be described by using the Brillouin function. The material does not get saturated even in a magnetic field of 50 kOe. From the fitting of 2 and 5 K data to the Brillouin function, the obtained saturation magnetization is estimated to be 2.2 emu/g. The total angular momentum J deduced from the fitting was found to be $J = 2.1$ at 5 K and $J = 1.8$ at 2 K. The expected value for Fe^{3+} is $J = 5/2$ (2.5) which agrees well with the 5 K data. The low absolute value of the Curie–Weiss temperature indicates that the Fe^{3+} magnetic moments interactions played an insignificant role in the investigated temperature regime. Similar findings were obtained for the 3% Co-doped TiO_2 sample, i.e., the material shows paramagnetic behavior within the whole temperature range measured. Inspecting the magnetic curves $\chi(T)$ and $M(H)$ displayed in Figs. 10(a) and (b), a remarkable feature can be noticed. At a certain temperature and magnetic field strength, the values of the magnetic susceptibility and the magnetization are significantly higher for the Co-doped TiO_2 synthesized from $Ti(OiPr)_4$ than for the one prepared using $TiCl_4$ as precursor. Applying the same procedure as in the case of iron, the cobalt concentration was determined to be 1.6 wt% (0.7 at%) for Co-doped TiO_2 prepared from $Ti(OiPr)_4$, and 0.04 wt% (0.02 at%) for Co-doped titania made from $TiCl_4$. The absence of interactions between the magnetic atoms (dopants) implies the absence of any ferromagnetism in the Fe- and Co-doped TiO_2 nanoparticles due to the low solubility of the dopants in the titania matrix or negligible concentration of oxygen vacancies.

4. Concluding remarks

In spite of all the progress in nanoparticle synthesis, many open questions remain to be answered. There is still an unpleasant lack of generally valid concepts or basic underlying mechanistic principles that would allow a rational synthesis planning. Liquid-phase routes in organic solvents offer a unique opportunity to chemists to control the structural, compositional, and morphological characteristics of colloidal inorganic nanoparticles [7–9], because they make it possible to influence the transformation of the precursor to the final inorganic nanomaterial on a molecular level, although yet in an empirical way [11]. Without any doubts, there is still a long way to go before nanoparticle formation and crystallization will be understood in all details. However, due to the slow reaction rates and due to the fact that organic reaction pathways are easier to study by standard techniques than aqueous systems, nonaqueous routes offer a great potential to elaborate chemical formation mechanisms. In addition to these mechanistic aspects, nonaqueous routes have already been proven to be particularly successful for a broad family of inorganic nanoparticles. In this article, we highlighted three important advantages based on selected examples: (i) preparation of doped and multi metal oxide nanocrystals without any postsynthetic heat treatment, (ii) tailoring of the crystal size and shape by organic species,

either present in the initial reaction solution or formed *in situ* during the reaction course, and (iii) possibility to obtain unusual crystal structures not found in the corresponding bulk material. These examples also strongly underline the importance of a careful characterization of both the inorganic nanoparticles and the organic reaction pathways.

Acknowledgments

Financial support from ETH Zürich is gratefully acknowledged. We also thank Prof. Robert Schlögl and Dr. Dang Sheng Su from the Fritz-Haber-Institute (FHI) in Berlin for the use of the electron microscope, and Antje Völkel (Max-Planck-Institute of Colloids and Interfaces, Potsdam) for the AUC measurement.

References

[1] B.L. Cushing, V.L. Kolesnichenko, C.J. O'Connor, Chem. Rev. 104 (2004) 3893.
[2] J. Livage, M. Henry, C. Sanchez, Prog. Solid State Chem. 18 (1988) 259.
[3] J.-P. Jolivet, C. Froidefond, A. Pottier, C. Chaneac, S. Cassaignon, E. Tronca, P. Euzen, J. Mater. Chem. 14 (2004) 3281.
[4] R.L. Brutchey, D.E. Morse, Angew. Chem. Int. Ed. 45 (2006) 6564.
[5] A. Dessombz, D. Chiche, P. Davidson, P. Panine, C. Chaneac, J.P. Jolivet, J. Am. Chem. Soc. 129 (2007) 5904.
[6] J. Yahiro, Y. Oaki, H. Imai, Small 2 (2006) 1183.
[7] Y.W. Jun, J.S. Choi, J. Cheon, Angew. Chem. Int. Ed. 45 (2006) 3414.
[8] J. Park, J. Joo, S.G. Kwon, Y. Jang, T. Hyeon, Angew. Chem. Int. Ed. 46 (2007) 4630.
[9] M. Niederberger, Acc. Chem. Res. 40 (2007) 793.
[10] C. de Mello Donega, P. Liljeroth, D. Vanmaekelbergh, Small 1 (2005) 1152.
[11] M. Niederberger, G. Garnweitner, Chem. Eur. J. 12 (2006) 7282.
[12] M. Niederberger, G. Garnweitner, J. Ba, J. Polleux, N. Pinna, Int. J. Nanotechnol. 4 (2007) 263.
[13] N. Pinna, M. Niederberger, Angew. Chem. Int. Ed. (2008) in press, doi:10.1002/anie.200704541.
[14] G. Garnweitner, M. Niederberger, J. Mater. Chem. 18 (2008) 1171.
[15] I. Djerdj, D. Arcon, Z. Jaglicic, M. Niederberger, J. Phys. Chem. C 111 (2007) 3614.
[16] I. Djerdj, G. Garnweitner, D.S. Su, M. Niederberger, J. Solid State Chem. 180 (2007) 2154.
[17] J. Rodriguez-Carvajal, Physica B 192 (1993) 55.
[18] J. Ba, D. Fattakhova Rohlfing, A. Feldhoff, T. Brezesinski, I. Djerdj, M. Wark, M. Niederberger, Chem. Mater. 18 (2006) 2848.
[19] M. Niederberger, G. Garnweitner, N. Pinna, M. Antonietti, J. Am. Chem. Soc. 126 (2004) 9120.
[20] V. Petkov, M. Gateshki, M. Niederberger, Y. Ren, Chem. Mater. 18 (2006) 814.
[21] M. Cao, I. Djerdj, M. Antonietti, M. Niederberger, Chem. Mater. 19 (2007) 5830.
[22] L. Zhang, G. Garnweitner, I. Djerdj, M. Antonietti, M. Niederberger, Chem. Asian J. 3 (2008) 746.
[23] G. Garnweitner, M. Niederberger, J. Am. Ceram. Soc. 89 (2006) 1801.
[24] X. Wang, Y. Li, Angew. Chem. Int. Ed. 41 (2002) 4790.
[25] R.L. Penn, J.F. Banfield, Am. Mineral. 83 (1998) 1077.
[26] C. Pacholski, A. Kornowski, H. Weller, Angew. Chem. Int. Ed. 41 (2002) 1188.
[27] Z. Tang, N.A. Kotov, Adv. Mater. 17 (2005) 951.
[28] M. Niederberger, H. Cölfen, Phys. Chem. Chem. Phys. 8 (2006) 3271.
[29] C. Ribeiro, C. Vila, J.M. Elias de Matos, J. Bettini, E. Longo, E.R. Leite, Chem. Eur. J. 13 (2007) 5798.
[30] M. Ghosh, K. Biswas, A. Sundaresan, C.N.R. Rao, J. Mater. Chem. 16 (2006) 106.
[31] A.L. Goodwin, M.G. Tucker, M.T. Dove, D.A. Keen, Phys. Rev. Lett. 96 (2006) 0472091.
[32] Y. Matsumoto, M. Murakami, M. Shono, T. Hasegawa, T. Fukumura, M. Kawasaki, P. Ahmet, T. Chikyow, S. Koshihara, H. Koinuma, Science 291 (2001) 854.
[33] Y. Matsumoto, R. Takahashi, M. Murakami, T. Koida, X.J. Fan, T. Hasegawa, T. Fukumura, M. Kawasaki, S. Koshihara, H. Koinuma, Jpn. J. Appl. Phys. 40 (Part 2) (2001) L1204.
[34] N. Hong, W. Prellier, J. Sakai, A. Hassini, Appl. Phys. Lett. 84 (2004) 2850.
[35] Y. Ding, W.Q. Han, L.H. Lewis, J. Appl. Phys. 102 (2007) 123902.
[36] J.D. Bryan, S.A. Santangelo, S.C. Keveren, D.R. Gamelin, J. Am. Chem. Soc. 127 (2005) 15568.
[37] Y.L. Soo, G. Kioseoglou, S. Kim, Y.H. Kao, P.S. Devi, J. Parise, R.J. Gambino, P.I. Gouma, Appl. Phys. Lett. 81 (2002) 655.
[38] N.H. Hong, J. Sakai, W. Prellier, A. Hassini, A. Ruyter, F. Gervais, Phys. Rev. B 70 (2004) 195204.
[39] L.F. Fu, N.D. Browning, S.X. Zhang, S.B. Ogale, D.C. Kundaliya, T. Venkatesan, J. Appl. Phys. 100 (2006) 123910.
[40] L. Balcells, C. Frontera, F. Sandiumenge, A. Roig, B. Martinez, J. Kouam, C. Monty, Appl. Phys. Lett. 89 (2006) 122501.
[41] S. Maensiri, P. Laokul, J. Klinkaewnarong, J. Magn. Magn. Mater. 302 (2006) 448.
[42] G. Clavel, M.G. Willinger, D. Zitoun, N. Pinna, Adv. Funct. Mater. 17 (2007) 3159.
[43] G. Clavel, M.G. Willinger, D. Zitoun, N. Pinna, Eur. J. Inorg. Chem. 2008 (2008) 863.
[44] H. Cölfen, T. Pauck, Colloid Polym. Sci. 275 (1997) 175.
[45] Y.W. Jun, M.F. Casula, J.H. Sim, S.Y. Kim, J. Cheon, A.P. Alivisatos, J. Am. Chem. Soc. 125 (2003) 15981.
[46] R.E. Tanner, Y. Liang, E.I. Altman, Surf. Sci. 506 (2002) 251.
[47] R.L. Penn, J.F. Banfield, Geochim. Cosmochim. Acta 63 (1999) 1549.
[48] R.L. Penn, J.F. Banfield, Science 281 (1998) 969.
[49] J. Polleux, N. Pinna, M. Antonietti, M. Niederberger, Adv. Mater. 16 (2004) 436.
[50] J. Polleux, N. Pinna, M. Antonietti, C. Hess, U. Wild, R. Schlögl, M. Niederberger, Chem. Eur. J. 11 (2005) 3541.